

PROTOPLANETARY DISK TURBULENCE DRIVEN BY THE STREAMING INSTABILITY: NON-LINEAR SATURATION AND PARTICLE CONCENTRATION

A. JOHANSEN¹

Max-Planck-Institut für Astronomie, 69117 Heidelberg, Germany

AND

A. YODIN²

Princeton University Observatory, Princeton, NJ 08544

Accepted for publication in ApJ

ABSTRACT

We present simulations of the non-linear evolution of streaming instabilities in protoplanetary disks. The two components of the disk, gas treated with grid hydrodynamics and solids treated as super-particles, are mutually coupled by drag forces. We find that the initially laminar equilibrium flow spontaneously develops into turbulence in our unstratified local model. Marginally coupled solids (that couple to the gas on a Keplerian time-scale) trigger an upward cascade to large particle clumps with peak overdensities above 100. The clumps evolve dynamically by losing material downstream to the radial drift flow while receiving recycled material from upstream. Smaller, more tightly coupled solids produce weaker turbulence with more transient overdensities on smaller length scales. The net inward radial drift is decreased for marginally coupled particles, whereas the tightly coupled particles migrate faster in the saturated turbulent state. The turbulent diffusion of solid particles, measured by their random walk, depends strongly on their stopping time and on the solids-to-gas ratio of the background state, but diffusion is generally modest, particularly for tightly coupled solids. Angular momentum transport is too weak and of the wrong sign to influence stellar accretion. Self-gravity and collisions will be needed to determine the relevance of particle overdensities for planetesimal formation.

Subject headings: diffusion — hydrodynamics — instabilities — planetary systems: protoplanetary disks — solar system: formation — turbulence

1. INTRODUCTION

This paper extends our preparatory numerical investigations of the streaming instability (Youdin & Johansen 2007, hereafter YJ) into the non-linear regime. The linear streaming instability was first described by Youdin & Goodman (2005, hereafter YG) who found that the radial and azimuthal drift of solids through gas in a protoplanetary disk triggers growing oscillations that concentrate particles. YJ details the numerical techniques used to study the evolution of solids and gas in a local patch of a protoplanetary disk and demonstrates that our code successfully reproduces the linear growth rates derived by YG. This paper describes the non-linear evolution of the streaming instability to a fully turbulent state and studies the consequences for particle concentration and transport.

The starward drift of solids, caused by the sub-Keplerian headwind encountered by the particles, is not just a trigger for streaming instabilities, but also a source of theoretical difficulties. Growing planetesimals by coagulation faces severe time-scale constraints due to the loss of solids (ultimately to the star or sublimation in the inner disk). The restriction is most acute for 10 cm “rocks” through 1 m “boulders” with drift times of only a few hundred orbits (Weidenschilling 1977a) in most of the

planet-forming region of standard minimum mass nebula models (Weidenschilling 1977b; Hayashi 1981). The drift of mm-sized solids in a few times 10^5 years at 30 AU is at best marginally consistent with the observed mm-excess from the outer parts of T-Tauri disks with ages of a few Myr (Wilner et al. 2000; Rodmann et al. 2006; see also Brauer et al. 2007 for possible ways to maintain such a population of “pebbles”). This mismatch between theory and observations may indicate that simple drift time estimates are missing important dynamical effects.

Several mechanisms could impede the radial influx of solids. The increased inertia of solids in a dense midplane sublayer decreases drift speeds as the local gas mass fraction squared (Nakagawa et al. 1986; Youdin & Chiang 2004). Since such high densities may trigger rapid gravitational collapse of solids (Youdin & Shu 2002), sedimentation alone is not a satisfactory explanation of the long lifetimes of pebbles in the disks, even if the turbulence is weak enough to allow the formation of an extremely thin mid-plane layer. Turbulent diffusion in accretion disks will maintain a small fraction of particles in the outer disk (Stepinski & Valageas 1996; Takeuchi & Lin 2002), but this scenario requires a particle reservoir that exceeds by far the observed amount of mm-sized solids and thus implies disk masses that are orders of magnitude larger than minimum mass models. Giant anticyclonic vortices (Barge & Sommeria 1995; de la Fuente Marcos & Barge 2001) stall migration by trapping marginally coupled solids. However the formation and stability of vortices in disks is not clear (Goodman et al. 1987; Klahr & Bodenheimer 2003; Johansen et al. 2004; Barranco & Marcus 2005;

Electronic address: johansen@mpia.de
Electronic address: youd@cita.utoronto.ca

¹ Visiting Astronomer, Department of Astrophysics, American Museum of Natural History

² Current address: Canadian Institute for Theoretical Astrophysics, University of Toronto, 60 Saint George Street, Toronto, ON M5S 3H8, Canada

Fromang & Nelson 2005). Any local pressure maximum – not only vortices – can trap boulders (Klahr & Lin 2001; Haghighipour & Boss 2003), e.g. spiral arms of massive self-gravitating disks (Rice et al. 2004) or even transient pressure enhancements in magnetorotational turbulence (Johansen et al. 2006b). The present work will show that streaming turbulence modestly slows the average radial drift of marginally coupled solids. An ultimate solution of the drift problem may require rapid (faster than drift) planetesimal formation (by gravitational collapse and/or coagulation) *and* fragmentation to maintain observed populations of small solids (Dullemond & Dominik 2005).

The dynamical particle trapping mechanisms mentioned above increase particle densities, with an efficiency that depends on (often uncertain) structure lifetimes. Local particle overdensities can seed gravitational collapse of solids and affect the rates of (and balance between) coagulation and collisional fragmentation. Optically thick clumps could even influence radiative transfer if the disk itself is optically thin, and thereby alter observational estimates of disk mass and particle size (see Draine 2006 for a general discussion of the role of optical depth, but not clumping *per se*). Radial drift inherently augments the surface density of solids in the inner disk as particles pile up from larger orbital radii, as long as particles are smaller than the gas mean free path so that Epstein drag applies (Youdin & Shu 2002; Youdin & Chiang 2004). In simulations and experiments of forced Kolmogorov turbulence, particles concentrate in low vorticity regions at the viscous dissipation scale (Fessler et al. 1994; Padoan et al. 2006). Efficient collection requires small particles that couple to the rapid turnover time at the dissipation scale. Cuzzi et al. (2001) apply this passive turbulent concentration to the size-sorting of chondrules (abundant, partially-molten, mm-sized inclusions found in primitive meteorites) in the inner solar nebula.

Johansen et al. (2006a) discovered active turbulent concentration (active meaning that the drag feedback on gas was included) of larger particles (from cm-sized pebbles to m-sized boulders) in simulations of Kelvin-Helmholtz midplane turbulence. Dense clumps of solids plow through the gas at near the Keplerian speed, scooping up more isolated particles that move with the sub-Keplerian headwind. Since this particle concentration mechanism relies on two-way drag forces, it was (and still is) considered a non-linear manifestation of streaming instabilities. The current work further explores active concentration, isolating the role of drag feedback by ignoring vertical stratification. We consider different geometries, both axisymmetric in the radial-vertical plane and fully 3-D, than Johansen et al. (2006a), who considered the azimuthal-vertical plane, and we use the higher order interpolation scheme for drag forces described in YJ. We will thus show that the “pure” streaming instability also produces strongly non-linear particle overdensities.

Turbulent diffusion controls the extent to which particles sediment in the mid-plane (Dubrulle et al. 1995) and whether (or how fast) self-gravity can collect solids into rings and bound clumps (Youdin 2005a,b). Diffusion is the most fundamental parameter governing whether planetesimals can form by gravitational instability (as originally proposed by Safronov 1969;

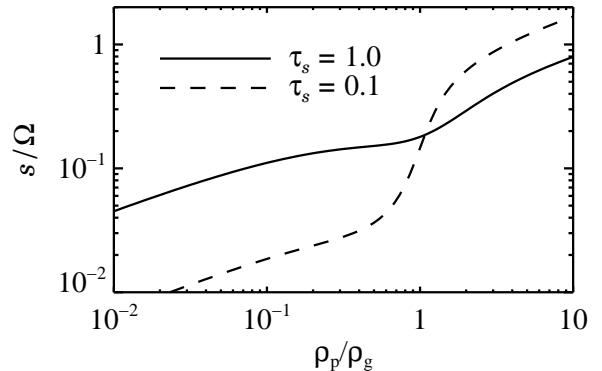


FIG. 1.— Peak growth rate s of the streaming instability versus the solids-to-gas ratio ϵ for friction times of $\tau_s = 1.0$ (solid line) and $\tau_s = 0.1$ (dashed line). The steep rise in growth rate when $\tau_s = 0.1$ particles cross $\rho_p/\rho_g = 1$ explains the cavitation in the non-linear run AB (see Fig. 5).

Goldreich & Ward 1973), because the oft-mentioned critical density for gravitational collapse is irrelevant when drag forces are included to transfer angular momentum from the solids to the gas (Ward 1976, 2000). Passive diffusion of particles in magnetorotational turbulence has been found to be quite strong (Johansen & Klahr 2005; Turner et al. 2006; Fromang & Papaloizou 2006; Carballido et al. 2006), although the Schmidt number (the ratio between the turbulent viscosity of the gas and the particle diffusion) increases in the presence of a net vertical magnetic field (Carballido et al. 2005; Johansen et al. 2006c). In the present work we measure the active particle diffusion in streaming turbulence, by considering the random walk of the particles away from a reference point, and find it to be relatively weak, especially for smaller particles.

The paper is built up as follows. In §2 we briefly reiterate the physical model of the protoplanetary disk and our numerical method for solving the dynamical equations of gas and solids. In §3 we present the non-linear simulations and the topography of the turbulent state, before analyzing in §4 the statistics and causes of particle clumping in more detail. Then §5 addresses the transport and diffusion of particles and angular momentum in the saturated streaming turbulence. We summarize our results in §6.

2. NUMERICAL METHOD

The dynamical equations and the numerical method are presented in detail in YJ, but we briefly recapitulate the main points in this section. As a numerical solver we use the Pencil Code³. This is a finite difference code that uses 6th order symmetric spatial derivatives and a 3rd order Runge-Kutta time integration (see Brandenburg 2003, for details).

We model a local patch in a protoplanetary disk with the shearing sheet approximation (e.g. Goldreich & Tremaine 1978). A Cartesian coordinate frame that corotates with the Kepler frequency Ω at a distance r from the central star is oriented with x , y and z axes pointing radially outwards, along the orbital direction, and vertically out of the disk (parallel to the

³ See <http://www.nordita.dk/software/pencil-code/>.

TABLE 1
RUN PARAMETERS

Run	τ_s	ϵ	$L_x \times L_y \times L_z$	$N_x \times N_y \times N_z$	N_p	Δt
AA	0.1	0.2	$4.0 \times 4.0 \times 4.0$	$256 \times 1 \times 256$	—	2000.0
AB	0.1	1.0	$2.0 \times 2.0 \times 2.0$	$256 \times 1 \times 256$	1.6×10^6	50.0
AC	0.1	3.0	$2.0 \times 2.0 \times 2.0$	$256 \times 1 \times 256$	1.6×10^6	50.0
BA	1.0	0.2	$40.0 \times 40.0 \times 40.0$	$256 \times 1 \times 256$	1.6×10^6	500.0
BB	1.0	1.0	$20.0 \times 20.0 \times 20.0$	$256 \times 1 \times 256$	1.6×10^6	250.0
BC	1.0	3.0	$20.0 \times 20.0 \times 20.0$	$256 \times 1 \times 256$	1.6×10^6	250.0
AB-3D	0.1	1.0	$2.0 \times 2.0 \times 2.0$	$128 \times 128 \times 128$	2.0×10^7	35.0
BA-3D	1.0	0.2	$40.0 \times 40.0 \times 40.0$	$128 \times 128 \times 128$	2.0×10^7	300.0

NOTE. — Col. (1): Name of run. Col. (2): Friction time. Col. (3): Solids-to-gas ratio. Col. (4): Box size in units of ηr . Col. (5): Grid resolution. Col. (6): Number of particles. Col. (7): Total run time in units of Ω^{-1} .

Keplerian angular momentum vector), respectively. We solve the equations of motion for deviations from Keplerian rotation in an unstratified model, i.e. vertical gravity is ignored. The gas (and not the solids) is subject to pressure forces, including the global radial pressure gradient, constant in the local approximation and measured by the dimensionless parameter

$$\eta \equiv -\frac{\partial P / \partial r}{2\rho_g \Omega^2 r} \approx \left(\frac{c_s}{v_K}\right)^2, \quad (1)$$

where $v_K = \Omega r$ is the Keplerian orbital speed, while P , ρ_g , and c_s are the pressure, density and sound speed of our isothermal gas. All our simulations use $\eta = 0.005$ and $c_s/v_K = H/r = 0.1$, where H is the gas scale-height. Our results can be applied to different values of η if velocities are scaled by ηv_K , the pressure-supported velocity, and lengths are scaled by ηr , the radial distance between points where Keplerian and pressure-supported velocities are equal.⁴

The solids are treated alternatively as a pressureless fluid or as superparticles that each contain the mass of many actual solid bodies. Solids and gas mutually interact by frictional drag forces that are linear in the relative velocity. This models small particles with a friction (or stopping) time τ_f that is independent of the relative speed between gas and particles (i.e. no turbulent wakes form). The translation from friction time to the radius of a particle depends only on gas properties and the material density of the solids. As a rule of thumb the radius of a compact icy particle in meters is roughly equal to the dimensionless stopping time

$$\tau_s \equiv \Omega \tau_f \quad (2)$$

at Jupiter’s location ($r \approx 5$ AU) in standard minimum mass nebula models (Hayashi 1981).

When solids are treated as numerical particles, we calculate the drag acceleration by interpolating the gas velocity at the positions of the particles using a second-order spline fit to the 9 (27) nearest grid points that surround a given particle for 2-D (3-D) grids. To conserve momentum we assign the drag force on each single particle back to the gas using a Triangular Shaped Cloud (TSC) scheme (Hockney & Eastwood 1981). This smoothing of the particles’ influence helps overcome shot

noise, and should not be seen as an SPH (smoothed particle hydrodynamics) approach since our particles carry no hydrodynamic properties. We showed in YJ that 1 particle per grid point is enough to resolve the linear growth of the streaming instability, but to better handle Poisson fluctuations for a wider range of densities, we generally use 25 particles per grid point in the non-linear simulations.

An equilibrium solution to the coupled equations of motion of the gas and the solids was found by Nakagawa et al. (1986, hereafter referred to as NSH) where drag balances the radial pressure gradient and Coriolis forces. YG found that this equilibrium triggered a linear drag instability. The peak growth rate of this streaming instability is shown in Fig. 1 as a function of the solids-to-gas ratio ϵ for τ_s of 0.1 and 1.0. See Figs. 1 and 2 of YJ (and the accompanying text) for the dependence of growth rates on wavenumber.

3. NON-LINEAR EVOLUTION TO TURBULENCE

With confidence from YJ that the code solves correctly for the linear growth of the streaming instability, we turn our focus to the non-linear evolution into turbulence. We generically refer to the non-linear states of our runs as “turbulent,” because they contain stochastic fluctuations that diffuse material and momentum. Some cases (the gas-dominated AA and BA runs, see below) appear more wave-like with peaks in the spatial and temporal Fourier spectra (as we will see in Fig. 12). However, even these runs exhibit diffusion and stochastic fluctuations on a range of scales, so we also label them as turbulent. This section describes the simulation parameters and main results for marginal vs. tighter coupling. More detailed analyses of the turbulent state follow in later sections.

3.1. Run Parameters and Initialization

The parameters of the different non-linear simulations are listed in Table 1. We consider two particle sizes, represented as friction times: tightly coupled solids with $\tau_s = 0.1$ (those runs are labeled A*, where * represents a solids-to-gas ratio label) and larger, more loosely coupled particles with $\tau_s = 1.0$ (labeled B*). Three values of the solids-to-gas mass ratio, $\epsilon = 0.2, 1.0, 3.0$ (labeled *A, *B, *C, respectively) are considered for each friction time. For instance model AB uses $\tau_s = 0.1$ and $\epsilon = 1.0$. The chosen particle abundances are well above the Solar composition of $\epsilon \sim 0.01$, but can very well be achieved in a sedimented mid-plane layer of solids, depending on

⁴ The value of $H/(\eta r)$ ($= 20$ in our simulations) changes with this scaling, but should not affect the results as long as Mach numbers remain low ($H/r \ll 1$) so that gas compressibility is insignificant.

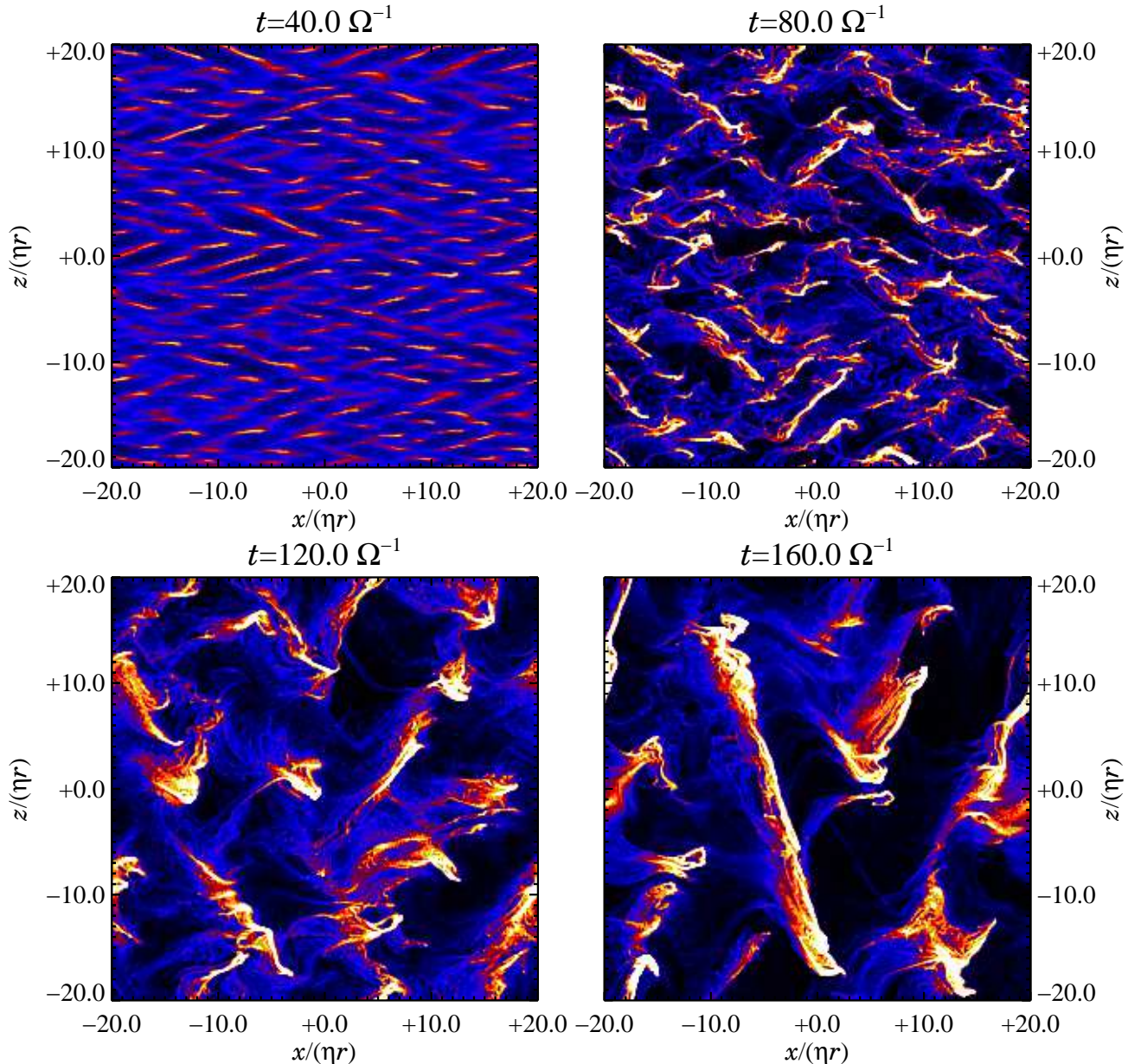


FIG. 2.— Particle density snapshots for run BA with friction time $\tau_s = 1.0$ and a solids-to-gas ratio of $\epsilon = 0.2$. Particle densities increase from black (zero density) to bright yellow/white (solids-to-gas of unity or higher). The evident linear wavelength in the first frame results from the streaming instability feeding off the drift of the particles through the gas. Subsequent frames document a surprising consequence of the self-consistently generated turbulence: the non-linear cascade of dense particle clumps into larger filaments.

turbulent diffusion and various particle enrichment or gas depletion mechanisms.

The size of the simulation box was chosen in all cases such that the most unstable radial wavelengths are resolved with at least 8 grid points. Two of the runs (labeled AB-3D, BA-3D) were fully 3-D, all others were 2.5-D simulations of the radial-vertical plane with all three velocity components, consistent with the linear analysis of YG. Fully periodic boundary conditions were used for the 2.5-D runs, while the 3-D simulations impose a shear-periodic boundary condition in the radial direction (see §3.2.1 of YJ). Particles are initially placed randomly throughout the simulation box. This “warm start” gives a white noise power spectrum with scale-independent Fourier amplitudes of $\tilde{\rho}_p(\mathbf{k})/\langle\rho_p\rangle \sim 1/\sqrt{N_p}$ in the particle density. The noise serves as a seed for streaming

instabilities. The velocities of gas and solids are initially set to the equilibrium values of NSH.

3.2. Marginally Coupled Boulders

Many drag force phenomena are most prominent for marginally coupled, $\tau_s = 1$, particles, corresponding to approximately meter-sized boulders at $r \approx 5$ AU in the solar nebula. Streaming instabilities are no exception, with fast linear growth⁵ and significant particle clumping in this regime. Fig. 2 shows four snapshots of the evolution of the streaming instability into turbulence for run BA ($\tau_s = 1.0$ $\epsilon = 0.2$). The initial growth is dominated by the fastest linear modes (first frame of Fig. 2), consistent with the maximum analytic growth rate, $s \approx 0.1\Omega$

⁵ Somewhat paradoxically, tight coupling gives faster growth in the particle-dominated regime, but on smaller scales.

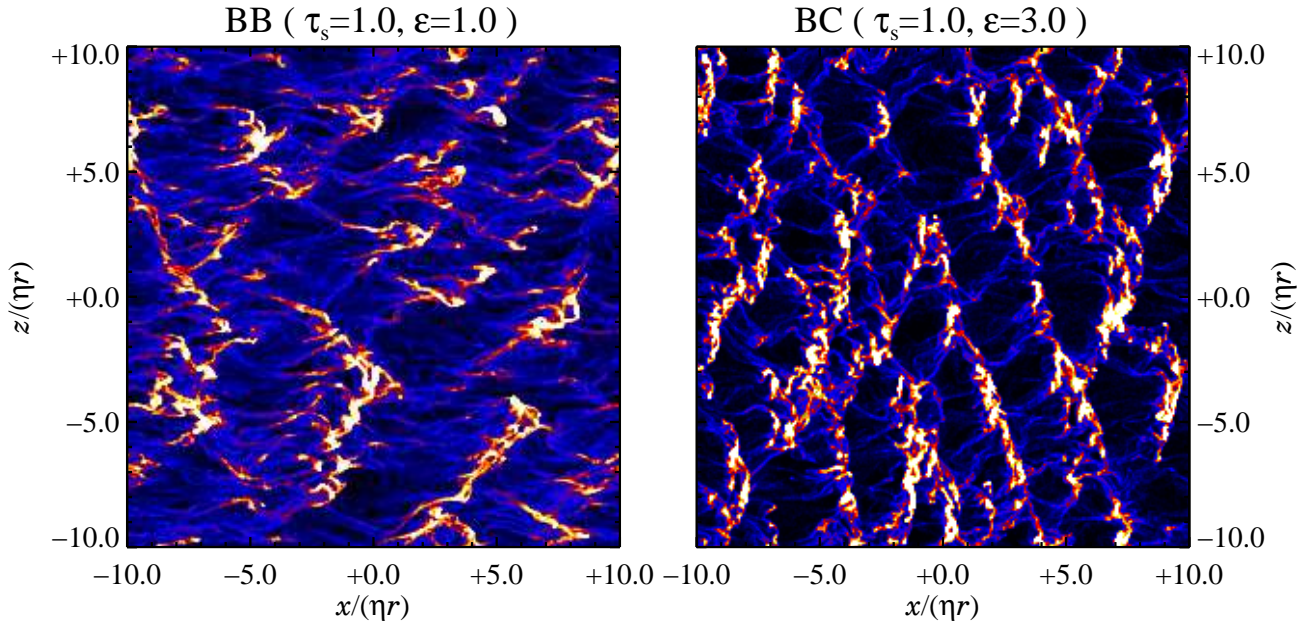


FIG. 3.— The saturated state of runs BB and BC (both at a time of $t = 100\Omega^{-1}$). The range of the solids-to-gas ratio is from 0-5 in the left plot and from 0-15 in the right plot, giving both the same relative scale for particle overdensities as Fig. 2. The tendency for dense clumps to lean against the radial drift flow is evident.

for $k_x \eta r \approx 1$ (see Fig. 1 and also Figs. 1 & 2 of YJ).

A non-linearly fluctuating, i.e. turbulent, state is reached after some 80 local shear times (second frame of Fig. 2). Solids become concentrated in a few massive clumps surrounded by an ocean of lower density material. Radial drift speeds are lower in such dense regions (we discuss the reduced radial drift further in §5.1). Solid particles are eventually lost downstream from the clumps into the voids, where the radial drift is faster, until they fall into another dense particle clump. Over a time-scale of more than 100 shear times (third and fourth frame of Fig. 2) this leads to an upward cascade of the density structure into extended filaments (actually rolls and sheets if we extend into the symmetric azimuthal dimension). The filaments are predominantly aligned in the vertical direction, which maximizes their ability to intercept particles, but are slightly tilted radially in alternating directions. Strong bulk motions are exhibited by the filaments along their long axis. This helps them stay upwind (motions are in the $+z, +x$ or $-z, +x$ directions), and leads to their disruption in several orbital times when alternately aligned filaments collide.⁶ The bulk motion also leads to efficient mixing of particles, especially in the vertical direction (see §5.3). The extended filaments are closely related to the long-lived vertically-oscillating clumps seen in 2-D simulations of the Kelvin-Helmholtz instability with $\tau_s = 1.0$ particles (see Fig. 8 of Johansen et al. 2006a).

The $\tau_s = 1.0$ runs with larger ϵ values (BB and BC) evolve similarly to run BA, but with a less pronounced cascade to larger scales (the saturated states of those two runs are shown in Fig. 3). Fig. 4 shows the evolution of maximum particle density (assigned with the TSC scheme to the grid) versus time for all three runs. The non-linear state is characterized by density peaks

⁶ The behavior described is best seen in a movie of run AB which can be downloaded from http://www.mpia.de/homes/johansen/research_en.php.

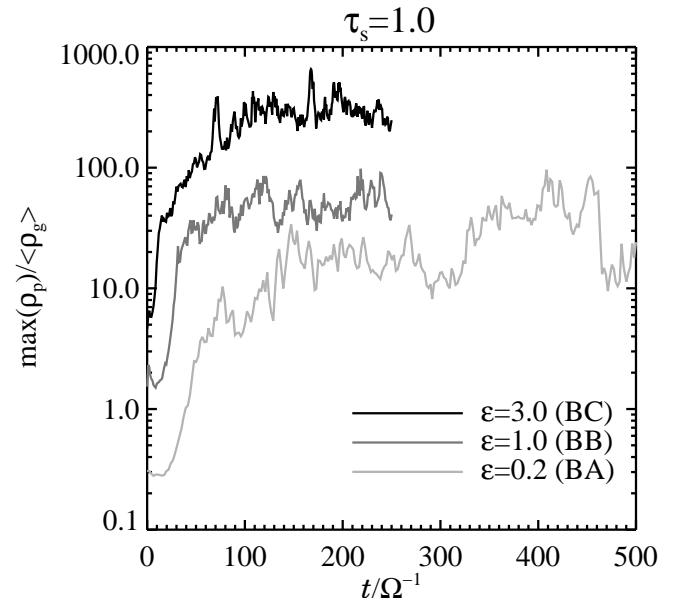


FIG. 4.— Maximum bulk density of solids, in units of the average gas density in the box, as a function of time for the three marginally coupled runs. The maximum density is generally around two orders of magnitude higher than the mean bulk density of the solids. The particle density has been assigned to the mesh using the TSC scheme.

100 times (or more) above the average particle density. Run BA has a longer run time, not only because the gas-dominated case is more astrophysically interesting, but also because it took longer to reach a saturated state. Fig. 4 shows signs of secular growth in densities over the entire $\Delta t = 500\Omega^{-1}$. Even longer runs would better characterize long term fluctuations in the saturated state, but such computational resources would probably be better spent on a more realistic model with vertical gravity.

Table 2 lists turbulent Mach numbers of the gas flow (after subtracting the mean flow, see §4.1). The

TABLE 2
 FLOW PROPERTIES

Run	τ_s	ϵ	Ma_x	Ma_y	Ma_z	$\overline{v_x}$	$\overline{v_x}^{(NSH)}$
AA	0.1	0.2	5.7×10^{-4}	1.1×10^{-3}	3.4×10^{-3}	-0.138	-0.138
AB	0.1	1.0	1.2×10^{-2}	6.1×10^{-3}	8.5×10^{-3}	-0.108	-0.050
AC	0.1	3.0	8.7×10^{-3}	4.5×10^{-3}	6.4×10^{-3}	-0.035	-0.012
BA	1.0	0.2	1.2×10^{-2}	1.8×10^{-2}	4.0×10^{-2}	-0.520	-0.820
BB	1.0	1.0	9.3×10^{-3}	1.1×10^{-2}	9.2×10^{-3}	-0.341	-0.400
BC	1.0	3.0	8.9×10^{-3}	1.3×10^{-2}	1.1×10^{-2}	-0.118	-0.118
AB-3D	0.1	1.0	5.3×10^{-3}	3.4×10^{-3}	2.7×10^{-3}	-0.064	-0.050
BA-3D	1.0	0.2	1.2×10^{-2}	1.7×10^{-2}	3.3×10^{-2}	-0.545	-0.820

NOTE. — Col. (1): Name of run. Col. (2): Friction time. Col. (3): Solids-to-gas ratio. Col. (4)-(6): Turbulent Mach number of the gas. Col. (7): Mean radial particle velocity in units of ηv_K . Col. (8): Mean radial particle velocity in NSH state.

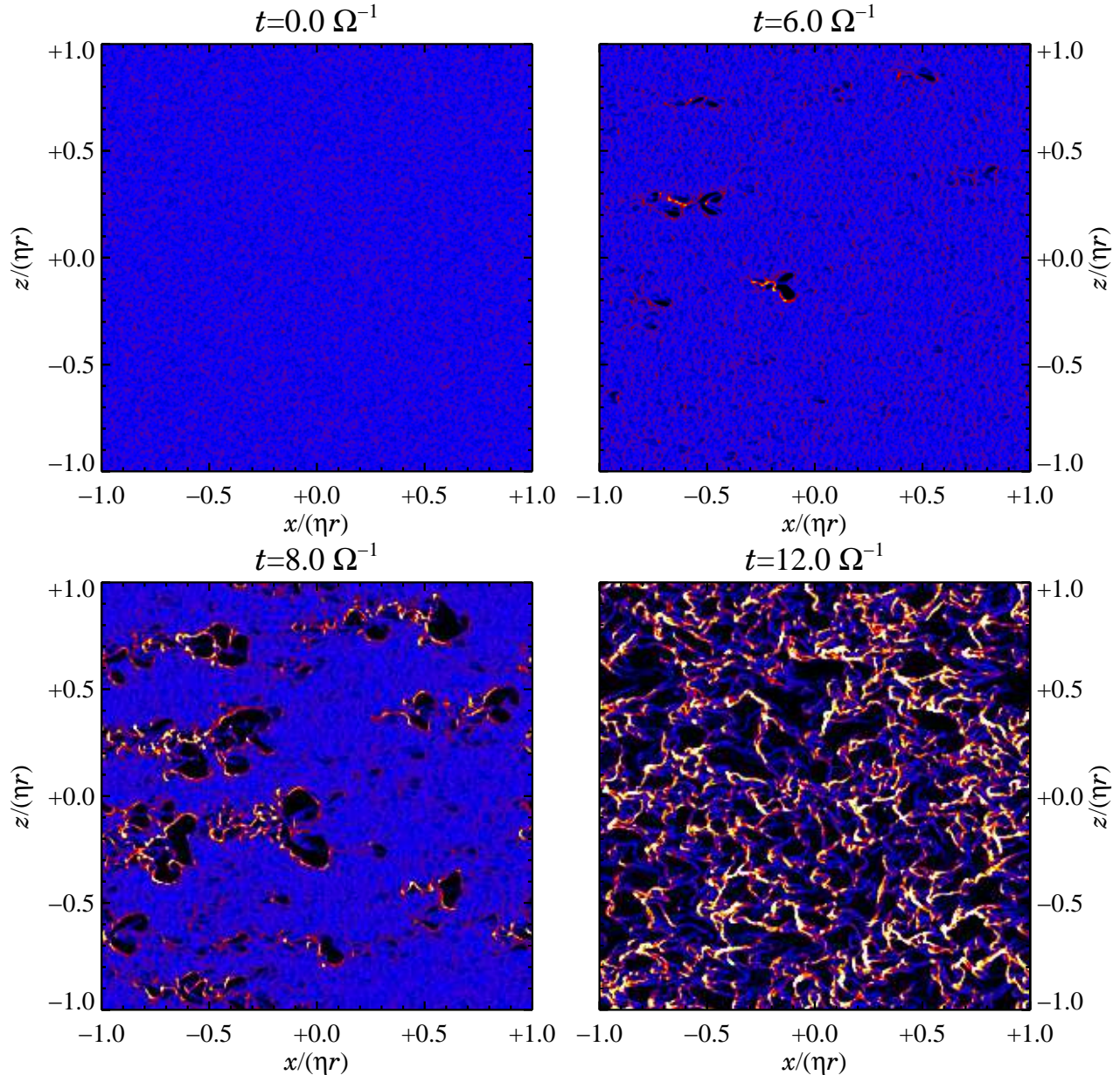


FIG. 5.— The onset of streaming turbulence for run AB ($\tau_s = 0.1$, $\epsilon = 1.0$). The plots show color coded particle density (black is zero particle density, bright is a solids-to-gas ratio of 5 or higher). The first frame shows only the initial Poisson noise. After around one orbital period small voids form. The inner edges of the cavities are loaded with particles that can fall rapidly through the voids in the absence of any collective drag force effects there. The voids rapidly expand, and a self-sustained turbulent state sets in after around 2 orbits. This atypical onset of turbulence is caused by an increased growth rate of the streaming instability in slightly overdense grid cells (see Fig. 1).

anisotropic turbulence of run BA, with stronger fluctuations in the vertical direction, is clear. Turbulence is more isotropic in the other marginally coupled runs.

3.3. Tightly Coupled Rocks

Simulations with shorter friction times are more costly because the shorter unstable length-scales (Figs. 1 & 2 of YJ) impose more stringent Courant criteria. The effort was nevertheless rewarded with a qualitatively very different behavior for the $\tau_s = 0.1$ runs. These particles correspond to solid rocks of approximately 10 cm size at $r = 5$ AU in the solar nebula.

3.3.1. $\tau_s = 0.1$, $\epsilon = 1.0$: Cavitation

Fig. 5 shows four snapshots of the particle density for run AB (friction time $\tau_s = 0.1$, solids-to-gas ratio $\epsilon = 1.0$). The first frame displays the initial Poisson noise. In contrast to run BA (see the first frame of Fig. 2), we do not see the smooth growth of linear waves over ten or more of orbital times (an expectation which follows from the peak growth rate $s \approx 0.15\Omega$). Instead a few voids with dense inner rims appear by $t = 6\Omega^{-1}$ (second frame). The cavities expand rapidly (third frame), leading to a fully turbulent state after only two orbits, i.e. $t \approx 12\Omega^{-1}$ (fourth frame).

The effect of Poisson fluctuations on the linear growth properties in Fig. 1 largely explains the surprisingly rapid and non-uniform growth. The $\epsilon = 1.0$ state lies amid a steep rise in growth rates from the gas-dominated to particle-dominated regimes. Specifically the growth time for $\epsilon = 1.0$, $t_{\text{grow}} \equiv 1/s = 6.8\Omega^{-1}$, is halved for a modest increase in the solids-to-gas ratio to $\epsilon = 1.25$. This enhanced growth applies in locally overdense regions. Poisson fluctuations from assigning $N_p = 1.6 \times 10^6$ particles to $N_b = 256^2$ bins generate density fluctuations with a standard deviation of $\delta_p \simeq \sqrt{N_b/N_p} \approx 0.2$. The TSC assignment smooths these fluctuations somewhat, but random overdensities 25% or greater still exist in over 1000 cells (1.6% of the total). Since a region with $\epsilon \approx 1.25$ is already non-linear after two e-foldings (consistent with the observed $t \approx 6\Omega^{-1}$), enhanced growth in overdense regions plausibly explains the growth of cavities.

We confirm this physical explanation for the cavities by running five variations to AB: (1) doubling the spatial resolution, (2) doubling the number of particles per grid cell, (3) seeding a linear mode (an eigenvector) with the “cold start” algorithm used for the linear tests in YJ, (4) the same linear mode, but the particle density distribution is seeded randomly (and thus dominated by Poisson fluctuations), and (5) quadratic polynomial instead of spline interpolation (see Appendix A of YJ). The growth of the root-mean-square of the vertical gas velocity for the first three variations is shown in Fig. 6 along with the original run BA. Variation (1) [and also (4) and (5), not shown] give essentially the same behavior run BA, which eliminates obvious numerical effects (grid resolution and interpolation scheme) as the source of cavities.⁷ Doubling the particle number, variation (2), delays the onset of cavitation, as expected with lower amplitude Poisson fluctuations. Variation (3) suppresses all Poisson noise, and the “cold” linear mode grows at the

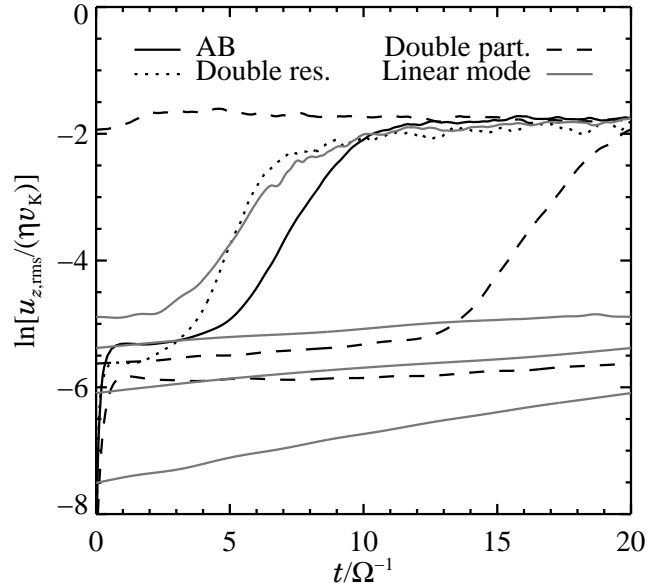


FIG. 6.— Growth of the streaming instability, as measured by the amplitude of vertical velocity fluctuations, for different numerical approaches to run AB. Only a seeded linear mode (gray line) grows with the expected growth rate of $s \approx 0.1\Omega$ (some curves have been wrapped around several times to allow simulations to run further). Fast growing cavities occur both at double resolution (dotted line) and with twice as many particles per grid cell (dashed line). Since cavities are triggered by Poisson density fluctuations, explosive growth is delayed with twice as many particles. The saturated state is the same for all cases.

analytic rate, $s \approx 0.1\Omega$, until non-linear effects finally dominate after $t = 60\Omega^{-1}$. Perhaps most importantly, all approaches lead to the same saturated state, despite markedly different routes to turbulence. This speaks to the robustness, not just of transient cavitation, but of all the non-linear results.

We also investigated the velocity structure at the onset of cavitation. Quadrupolar structures (most prominent in the vertical velocity) appear as isolated modes of the streaming instability. The length scale of the quadrupolar distortions did not vary upon doubling the grid resolution (with a fixed number of particles per grid cell).

Fortunately, our Poisson noise hypothesis does not predict cavitation where it should not occur. Run AC ($\tau_s = 0.1$, $\epsilon = 3.0$) has a fast linear growth rate with a relatively weak dependence on the local value of ϵ (see Fig. 1). Accordingly non-linear fluctuations appear uniformly throughout the grid in run AC, instead of cavitating first in a few spots. The saturated state of run AC (shown in the right panel of Fig. 7) is similar to run AB, but with smaller scale fluctuations. Like run AB, the marginally coupled run BB has equal densities of particles and gas, but with $\tau_s = 1.0$ the rise in growth rates across $\epsilon = 1$ was much smoother (see Fig. 1).⁸ Since the effect of Poisson fluctuations is weak (an overdensity of 25% only cuts the growth time by 12% for $\tau_s = 1.0$ instead of halving it for $\tau_s = 0.1$) run BB displays orderly growth of the dominant linear modes.

3.3.2. $\tau_s = 0.1$, $\epsilon = 0.2$: Weak Overdensities

Fig. 8 plots the maximum particle density versus time for the three tightly coupled simulations. The streaming

⁷ Variation (5) is interesting because the Poisson density fluctuations dominate the carefully seeded velocities.

⁸ Fig. 3 of YG confirms this trend, showing that the transition is yet sharper for $\tau_s = 0.01$ “pebbles.”

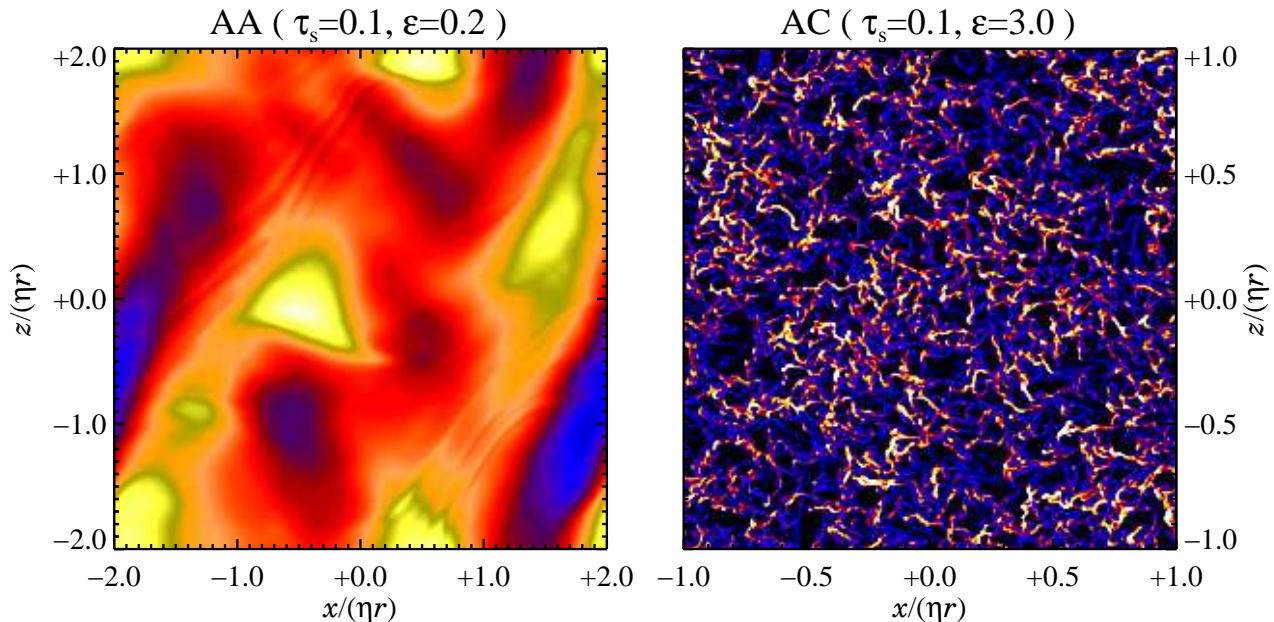


FIG. 7.— The saturated states of run AA (at $t = 1000\Omega^{-1}$) and run AC (at $t = 50\Omega^{-1}$). The range in solids-to-gas ratio is 0.15-0.25 in the left plot and 0-15 in the right plot. Run AA (calculated with the two fluid code, see §3.3.2 for explanation) is dominated by oscillatory motion of slightly overdense clumps. The turbulent state of run AC is very much like run AB, but at smaller scales. Also the non-linear state of run AC develops simultaneously throughout the grid, unlike the cavitation of run AB.

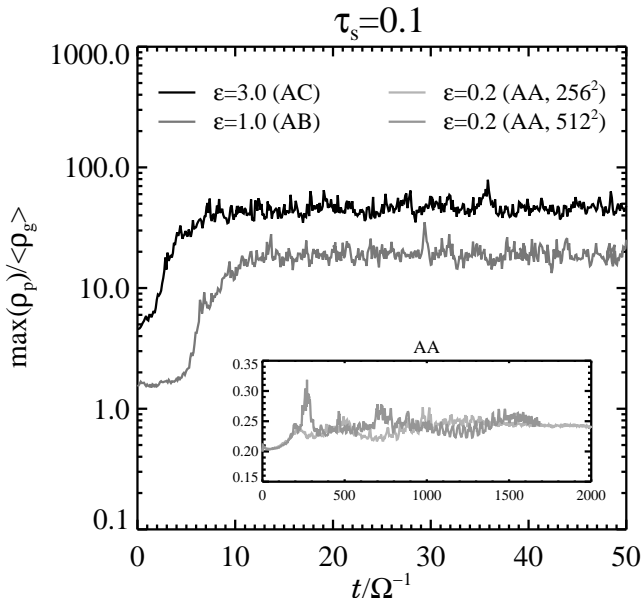


FIG. 8.— Maximum bulk density of solids for the three tightly coupled runs (AB, AC and in the insert AA at two different resolutions). The maximum density is around an order of magnitude higher than the average for the $\epsilon = 1.0, 3.0$ runs, whereas the turbulent state of the $\epsilon = 0.2$ run only experiences very mild relative overdensities of around 20% at both 256^2 and 512^2 mesh resolution.

instability produces particle overdensities of 20 or more in runs AB and AC. However the gas-dominated case AA has a qualitatively different behavior. Growth saturates (see left panel of Fig. 7) in a few growth times, $t_{\text{grow}} = 1/s \approx 42\Omega^{-1}$, as expected. However the particle overdensities are very mild, only 20% on average (see inset of Fig. 8). To test for convergence we ran the simulation at both 256^2 and 512^2 grid points, but the qualitative evolution of maximum bulk density of solids is unchanged (after a small initial peak in the 512^2 run).

We emphasize that run AA was performed with the

two-fluid code, not the particle-fluid approach used in the other simulations. This choice was necessitated by computational cost of long growth times with short wavelengths that restrict the code to small time steps. It is tempting to suspect that the weak overdensities in AA are a consequence of the two-fluid approach. However the limitation of the pressureless fluid model of solids is that density gradients steepen and shock, causing numerical instabilities, *not* that they are stably smoothed. To confirm this we ran two-fluid simulations of case AB and obtained the expected (from the particle-fluid run) growth of particle density until the code crashed after the growth of non-linear overdensities. By contrast AA simply never generates large density fluctuations, apparently since drag feedback on the gas is too weak in the small particle, gas-dominated regime.

3.4. 3-D Simulations

We have also performed full 3-D simulations of the streaming instability with 128^3 grid points and $N_p = 2 \times 10^7$ particles. The linear analysis of YG assumed axisymmetry, partly for simplicity, but also because modes that grow slowly (with $s < \Omega$) will be sheared into rings in any event. Computer simulations are needed to determine whether the saturated state remains azimuthally symmetric in 3-D and how the presence of the azimuthal direction affects turbulent properties. Note that even axisymmetric linear instabilities can give rise to non-axisymmetric parasitic instabilities (e.g. Kelvin-Helmholtz instabilities that feed off the channel flow of the magnetorotational instability, see Goodman & Xu 1994).

Fig. 9 shows the particle density for runs BA-3D and AB-3D in a saturated state. The marginally coupled case (BA-3D) maintains a high degree of axisymmetry. The radial-vertical plane shows the cascade into sheets similar to the 2.5-D case (as seen in Fig. 2). The quantitative analysis of turbulent properties (see Tables 2 and

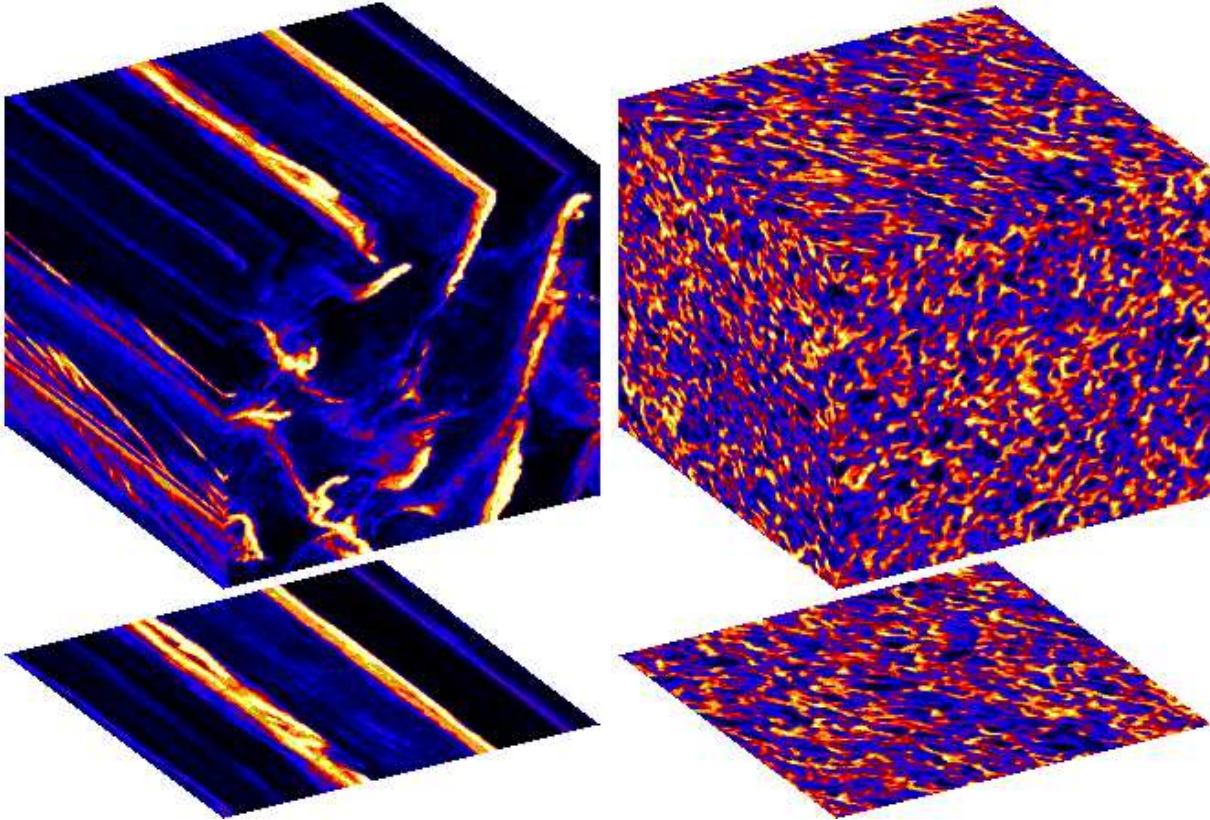


FIG. 9.— Saturated streaming turbulence for run BA-3D ($\epsilon = 0.2$, $\tau_s = 1.0$, left) and run AB-3D ($\epsilon = 1.0$, $\tau_s = 0.1$, right). The boxes are oriented with the radial x -axis to the right and slightly up, the azimuthal y -axis to the left and up, and the vertical z -axis directly up. The contours show the particle density at the sides of the simulation box after the streaming turbulence has saturated. The axisymmetry of the marginally coupled particles witnesses the smearing effect of Keplerian shear on the relatively long-lived clumps. The tightly coupled particles drive rapid fluctuations that develop fully non-axisymmetric density patterns.

3) confirms that BA-3D is very similar to the 2.5-D case. The ability to maintain azimuthal symmetry suggests (as we will confirm in §4.3) that particles reside in clumps for longer than an orbital time, so that clumps become azimuthally elongated by radial shear. Notice that the clump lifetime is not so long that structures appear perfectly axisymmetric.

The tightly coupled case (AB-3D) on the other hand evolves completely non-axisymmetrically. Indeed the correlation time of the clumps is short enough that they are not significantly elongated by Keplerian shear. Similar to the 2.5-D case, cavities (now fully 3-D and non-axisymmetric) developed out of the initial Poisson noise in run AB-3D. The saturated state appears to have less pronounced clumps than run AB (the fourth panel of Fig. 5). Tables 2 and 3 show that the 3-D turbulence indeed has lower velocities (Mach numbers) and weaker diffusion, particularly in the vertical direction. It is to be expected that turbulent properties in the 3-D runs change more for the case that is non-axisymmetric (AB-3D) than the case that remains axisymmetric (BA-3D) and was already capturing the relevant physics.

The peak particle densities for the two 3-D runs are shown in Fig. 10. Compared to the density evolution of the 2.5-D runs (Figs. 4 and 8) it is evident that BA-3D agrees well with BA, whereas AB-3D achieves a somewhat lower maximum density than AB does. We will focus most of our analysis on the 2.5-D runs because we could conduct a more systematic study of parameter space at higher spatial resolution. The 3-D runs pre-

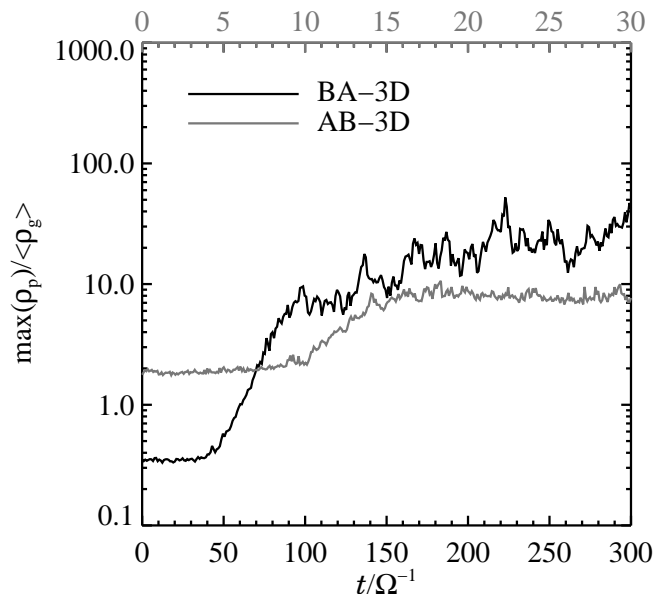


FIG. 10.— Evolution of the maximum bulk density of solids in the two 3-D simulations (notice the different time axes). The density of AB-3D is somewhat lower than in the 2.5-D case (Fig. 8), whereas the marginally coupled BA-3D shows good agreement with run BA in Fig. 4.

sented here support this choice by giving qualitatively (and for BA, fairly quantitatively) similar results to the 2.5-D runs.

TABLE 3
 TURBULENT TRANSPORT

Run	τ_s	ϵ	D_x	D_z	$\mathcal{F}_{\mathcal{L},x}^{(\text{turb})}$	$\mathcal{F}_{\mathcal{L},x}^{(\text{NSH})}$
AA	0.1	0.2	$(1.4 \pm 6.2) \times 10^{-7}$	$(6.0 \pm 262) \times 10^{-7}$	-2.2×10^{-8}	-4.8×10^{-7}
AB	0.1	1.0	$(4.4 \pm 0.4) \times 10^{-5}$	$(2.9 \pm 0.5) \times 10^{-5}$	-6.1×10^{-5}	-3.1×10^{-7}
AC	0.1	3.0	$(2.0 \pm 0.2) \times 10^{-5}$	$(1.8 \pm 0.2) \times 10^{-5}$	-6.0×10^{-5}	-5.8×10^{-8}
BA	1.0	0.2	$(2.2 \pm 0.6) \times 10^{-3}$	$(1.5 \pm 0.8) \times 10^{-2}$	6.7×10^{-5}	-1.7×10^{-4}
BB	1.0	1.0	$(7.6 \pm 0.7) \times 10^{-4}$	$(1.7 \pm 0.4) \times 10^{-4}$	-4.0×10^{-5}	-2.0×10^{-4}
BC	1.0	3.0	$(2.8 \pm 0.2) \times 10^{-4}$	$(6.2 \pm 0.9) \times 10^{-4}$	-1.5×10^{-4}	-5.2×10^{-5}
AB-3D	0.1	1.0	$(1.6 \pm 0.2) \times 10^{-5}$	$(2.7 \pm 0.1) \times 10^{-6}$	-1.5×10^{-5}	-3.1×10^{-7}
BA-3D	1.0	0.2	$(2.0 \pm 0.3) \times 10^{-3}$	$(8.2 \pm 2.5) \times 10^{-3}$	6.0×10^{-5}	-1.7×10^{-4}

NOTE. — Col. (1): Name of run. Col. (2): Friction time. Col. (3): Solids-to-gas ratio. Col. (4)-(5): Turbulent diffusion coefficient in units of $c_s^2 \Omega^{-1}$ (interval indicates one standard deviation in each direction). Col. (6): Radial flux of azimuthal momentum relative to NSH state. Col. (7): Radial flux of azimuthal momentum in NSH state. All quantities are normalized with standard combinations of Ω , c_s and ρ_g .

The ability of drag forces to concentrate particles via the non-linear evolution of the streaming instability is now analyzed in detail. This fundamentally important process could alter the collisional evolution of the size spectrum of particles, leading to an enhanced growth of the average particle radius, or even trigger gravitational instabilities in the solid component of protoplanetary disks.

4.1. Gas Does Not Clump

We emphasize that gas densities remain nearly constant, despite non-linear particle overdensities in streaming turbulence. Gas overdensities are $\lesssim 1\%$ in all runs. This validates our use of a constant stopping time, τ_f (which would otherwise vary with gas density in the Epstein regime). We note that the linear analysis of YG assumed a perfectly incompressible gas. YJ confirmed that the linear growth is indeed unaffected by gas compressibility, which we now see also remains weak in the non-linear regime.

The gas fluctuations are consistent with the small Mach numbers in Table 2, which are below (but near) the scale set by the pressure supported velocity, ηv_K , with $\eta v_K / c_s = 0.05$ in our simulations. Curiously, the range in *radial* Mach numbers is remarkably narrow for all the 2.5-D simulations, from 8.7×10^{-3} to 1.2×10^{-2} (with the weakly turbulent, two-fluid run AA excluded).

4.2. Particle Density Distribution

To get a clear picture of both typical and maximum particle overdensities, Fig. 11 plots the cumulative distributions of particle density during the saturated phase of the simulations. The distributions measure the fraction of particles with ambient densities above a given value, and are averaged over many snapshots to ensure adequate sampling. Particle densities relative to the gas are readily obtained by multiplying the x -axis values by $\epsilon = \langle \rho_p \rangle / \langle \rho_g \rangle$. Run BA ($\tau_s = 1.0$, $\epsilon = 0.2$) has the largest particle overdensities, of nearly 1000, meaning ρ_p reaches nearly 200 times the gas density. However since run BC ($\tau_s = 1.0$, $\epsilon = 3.0$) starts with a particle density 15 times larger, it experiences larger peak values of $\rho_p / \langle \rho_g \rangle \approx 900$. Curiously run BB ($\tau_s = 1.0$, $\epsilon = 1.0$) is not an intermediate case but has smaller overdensities relative to both particles and gas.

Particle concentration is more modest during the

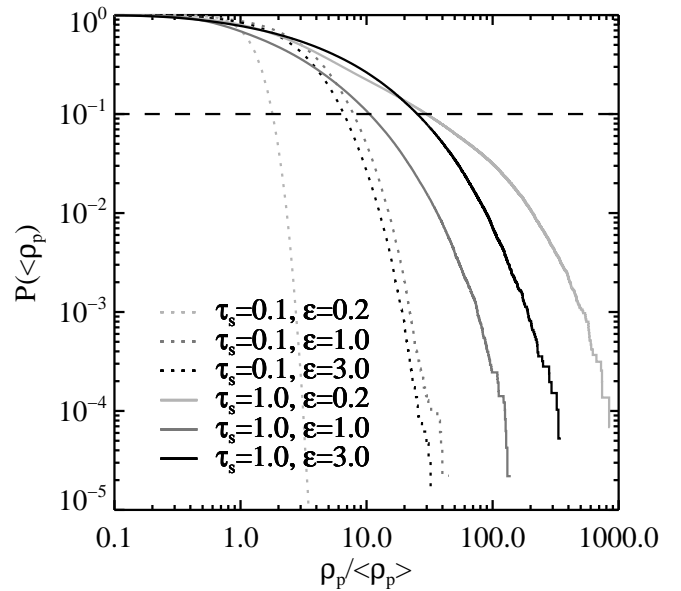


FIG. 11.— Cumulative particle density distributions. The curves show the fraction of particles with an ambient density $\geq \rho_p$ (the dashed line indicates a 10% border between typical and exceptional). Except for run AA ($\tau_s = 0.1$, $\epsilon = 0.2$) the majority of particles reside in clumps overdense by a factor of 2–10. A small fraction of particles experience extreme overdensities of nearly 1000.

tightly coupled runs. Case AB and AC have very similar particle overdensities, with an average $\delta_p \approx 2-3$ and a peak $\delta_p \approx 30$. For case AA ($\tau_s = 0.1$, $\epsilon = 0.2$) the overdensities are negligible. It is remarkable (if a bit mysterious) that the $\epsilon = 0.2$ runs give both the strongest (BA) and weakest (AA) particle overdensities, depending on stopping time!

Fourier spectra of the particle density are shown in Fig. 12. The absolute value of the Fourier amplitudes, normalized by the mean bulk density of particles, has been averaged over many snapshots during the saturated turbulent state of the simulations. Runs BA, BB and BC show clear peaks at large scales in agreement with the scale of the clumps seen in Figs. 2 and 3, whereas the power in the tightly coupled runs AB and AC is largely isotropic and monotonically decreasing with decreasing wave length. Run AA is extremely dominated by the very largest scales of the box.

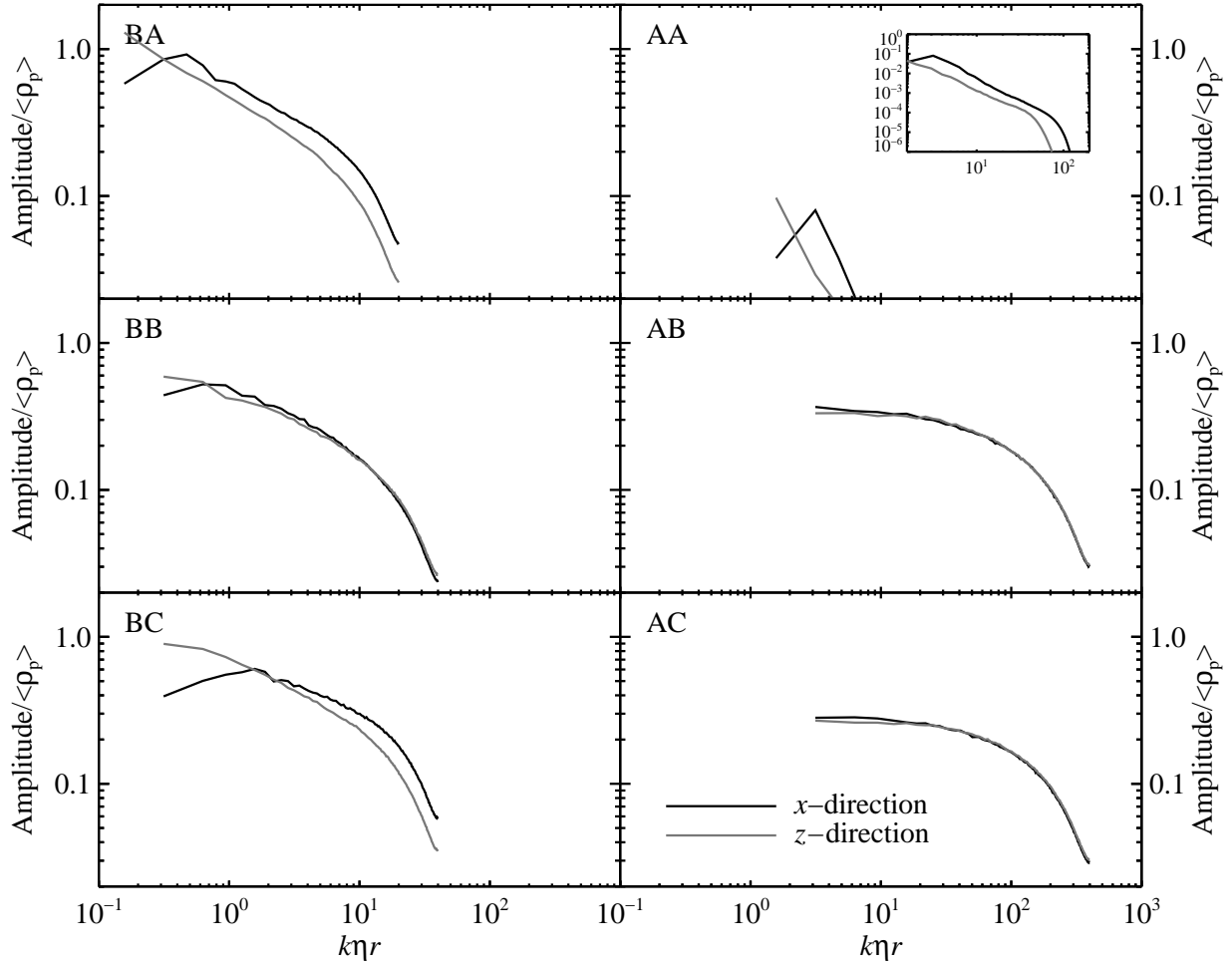


FIG. 12.— Power spectra of the bulk particle density, along the x -direction (black line) and the z -direction (gray line). The Fourier amplitudes are shown normalized with the mean density of particles in each simulation. Runs BA, BB and BC show clear peaks at large scales in agreement with the scale of the clumps seen in Figs. 2 and 3, whereas the power in the tightly coupled runs AB and AC is largely isotropic and monotonically decreasing with decreasing wave length. Run AA is extremely top heavy with power almost exclusively at the few largest scales of the box (see insert).

4.3. Correlation Times

The residence time of particles in dense clumps affects the cosmogonical processes, e.g. gravitational collapse or chondrule formation, that might occur therein. For this purpose, we measure the time correlation function of the ambient density, $\rho_p^{(i)}$, experienced by particle i ,

$$C_\rho(t) = \langle \rho_p^{(i)}(t') \rho_p^{(i)}(t' + t) \rangle - \langle \rho_p^{(i)} \rangle^2, \quad (3)$$

from snapshots of the particle positions taken every $\Delta t = \Omega^{-1}$ apart. The brackets indicate an average over time⁹ and the particles tracked (10% of the total was more than sufficient for convergence). Subtraction of the mean squared $\rho_p^{(i)}$ ensures that positive (negative) values of $C_\rho(t)$ correspond to correlation (anticorrelation), respectively.

Fig. 13 plots the time correlation function for the saturated state of the 2.5-D simulations. A characteristic correlation time, t_{corr} , is obtained when C_ρ drops to half

⁹ Since averaging is restricted to intervals t apart, the largest t considered is never more than half the (non-linearly saturated) duration of the simulation.

its peak value.¹⁰ Runs BA and BC have the longest $t_{\text{corr}} \approx (6-7)\Omega^{-1}$. Run BA is the best sampled and shows a secondary peak past $t = 60\Omega^{-1}$ indicating either periodicity or (more likely) secular changes from the ongoing cascade and small clump numbers. Run BB enjoys a shorter $t_{\text{corr}} \approx 3.5\Omega^{-1}$, but C_ρ does not quite drop to zero, an indication that a fraction of particles remain in dense regions.

The runs with tighter coupling of $\tau_s = 0.1$ (AB and AC) had quite short $t_{\text{corr}} \approx 0.7\Omega^{-1}$ (note the compressed time axis in Fig. 13 for these runs). The short correlation times are consistent with the less pronounced clumping and lack of upward cascade when compared to the marginally coupled runs. For run AC, C_ρ is significantly negative for $t > 20\Omega^{-1}$, indicating that particles avoid dense clumps after leaving them.

It is clear from movies of the simulations that many clumps persist longer than t_{corr} , particularly in the marginally coupled $\tau_s = 1.0$ runs. The particles that make up a clump continuously leak out downstream to

¹⁰ We considered defining correlation functions and times only for particles initially residing in overdense regions, but equation (3) is a quadratic measure that already favors such regions. The simpler, more standard definition is sufficient for our purposes.

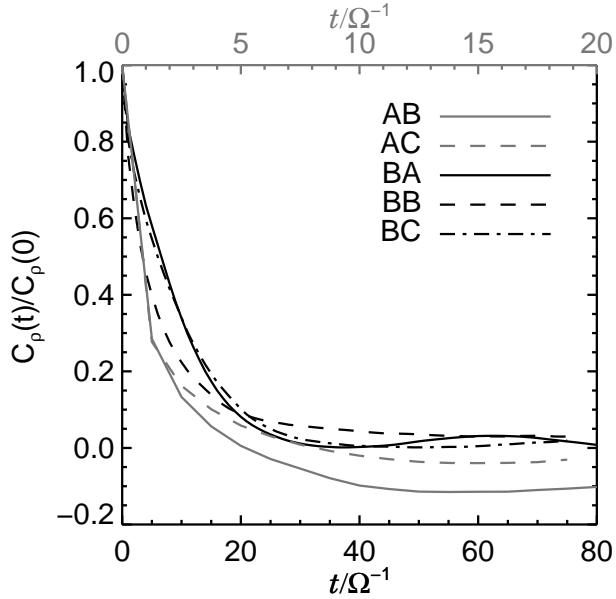


FIG. 13.— Time correlation functions for particle density indicate how long particles reside in dense clumps. Runs BA and BC have long correlation times of $\sim 7\Omega^{-1}$, while BB has a slightly shorter value of $3.5\Omega^{-1}$. These $\tau_s = 1.0$ runs use black lines and the lower black time axis. The tightly coupled runs, AB and AC (gray lines and the upper gray compressed time axis), have very short correlation times $< 1\Omega^{-1}$.

the radial drift flow and are replaced with new particles drifting in from upstream. The mismatch between clump lifetime and density correlation time is evidence that the clumps are a dynamical, collective phenomenon in the solid component, rather than a persisting density enhancement. That situation might change with the inclusion of the self-gravity of the solid particles, as this could cause the clumps as a whole to collapse under their own weight, fragmenting perhaps into gravitationally bound objects. We plan to include the self-gravity of the particles in a future research project.

4.4. Energetics of Clumping

The growth of particle clumps shields solids from the full brunt of drag forces, akin to the drafting practiced in bicycle pelotons. In YJ §5.1 we show that the rate of energy dissipation by drag forces,

$$\dot{\mathcal{E}}_{\text{drag}} = -\rho_p |\mathbf{v}_g - \mathbf{v}_p|^2 / \tau_f, \quad (4)$$

is diminished (brought closer to zero) by particle clumping in the laminar state (at least for tight or marginal coupling). To determine the relevance of this process for the saturated turbulent state, Fig. 14 plots the time evolution of the energy dissipation rate for the marginally coupled runs (black time axis) and two of the tightly coupled runs (gray time axis). For the tightly coupled runs (AB and AC) the dissipation actually becomes stronger (more negative) in the saturated state, a consequence of increased relative velocities in the turbulent state. Since these runs also have significant overdensities, the lowering of $|\dot{\mathcal{E}}_{\text{drag}}|$ is apparently not a necessary condition for clumping. The short clump lifetimes (see Fig. 13) is consistent with the inability to reduce dissipation by drafting for $\tau_s = 0.1$.

By contrast, all marginally coupled runs (BA, BB and BC) show diminished dissipation in the non-linear

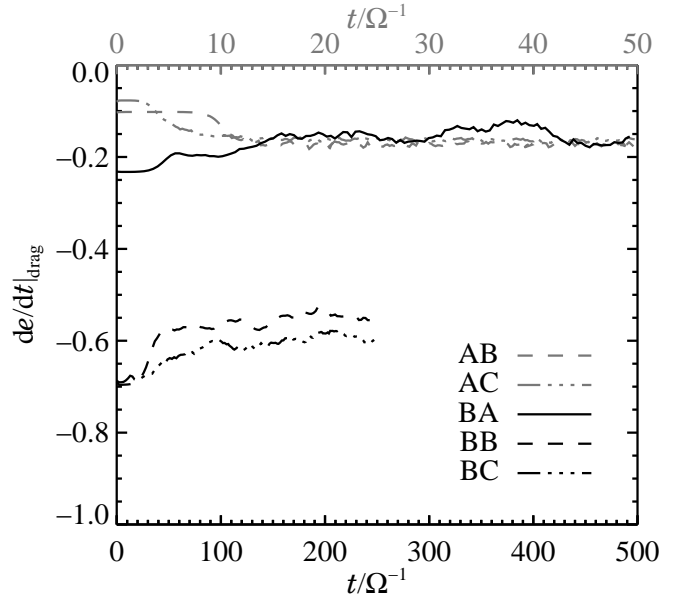


FIG. 14.— The energy dissipation rate [normalized to $(\rho_g)(\eta v_K)^2 \Omega$] from drag forces between solids and gas. Marginally coupled runs BA, BB and BC (black curves) reduce the dissipation rate in the turbulent state, by shielding particles in dense, long-lived particle clumps. Tightly coupled runs AB and AC (gray curves, which follow the top gray compressed time axis) show increased dissipation, since particle clumps are too short-lived to allow such shielding.

state, more consistent with the analytic expectations from clumps in a laminar flow. The longer correlation times and the upward cascade into large clumps exhibiting bulk motion (particularly in AB, see §3.2) foster the reduction of $|\dot{\mathcal{E}}_{\text{drag}}|$. The resulting particle overdensities are significantly larger for these $\tau_s = 1.0$ runs (see Fig. 11). Thus diminishing drag dissipation is not required to generate particle overdensities, but this drafting mechanism can augment the growth of dense clumps.

5. TRANSPORT

In this section we quantify the effect of the streaming turbulence on the radial drift of particles, radial momentum transport and on the diffusive mixing of solids.

5.1. Radial Drift

We initially expected that streaming turbulence would reduce the radial migration of particles, due to the pronounced particle clumping. The laminar drift of particles slows as [see YJ equation (7c)]

$$w_x^{(\text{NSH})} = -\frac{2\tau_s}{(1 + \rho_p/\rho_g)^2 + \tau_s^2} \eta v_K \quad (5)$$

$$\rightarrow -\left(\frac{\rho_p}{\rho_g}\right)^2 2\eta v_K \tau_s \text{ for } \frac{\rho_p}{\rho_g} \gg 1, \tau_s \quad (6)$$

with increasing particle inertia. The results of the simulations are more complicated since turbulent velocity fluctuations produce drift speeds that deviate from local equilibrium.

Table 2 lists average radial drift velocities in the turbulent state, along with the laminar equilibrium values from NSH. Radial drift decreases by about 40% during run BA, as is also shown in Fig. 15. For the other $\tau_s = 1.0$ runs, BB displays a modest 15% reduction while BC is

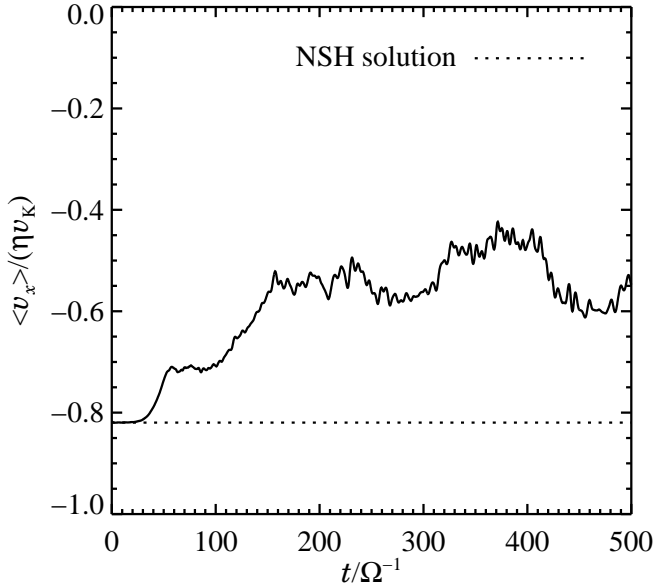


FIG. 15.— Evolution of the radial drift speed of solids during run BA, averaged over all 1,600,000 particles. Streaming turbulence slows the influx of solids by 40% below the laminar drift speed (dotted line) on average, with significant temporal fluctuations that correlate with peaks in the maximum bulk density of particles (Fig. 4).

unchanged despite significant overdensities. The tightly coupled runs show marked increases in drift speeds of 200% for AB and 300% for AC. Note that BA has the fastest laminar drift (due to marginal coupling and low solids-to-gas ratio), while AC (followed by AB) have the slowest laminar drift (because of tight coupling and large particle inertia). While the same ordering of drift speeds holds in the turbulent state, the range of speeds for different parameter choices shrinks (i.e. the fastest slow down and the slowest speed up). We examine this trend in detail below.

Fig. 16 shows (with black histograms) the distribution of drift velocities, averaged over time in the turbulent state, for six different runs. For comparison, the location of the equilibrium drift velocity is indicated with a short vertical line (labeled NSH). The full gray lines plot the average ambient particle density for particles in a given velocity bin, and should be compared to the dash-dotted gray lines that show the laminar relation between particle density and drift velocity (from the inversion of eq. [5]). The laminar drift velocities have a finite range from 0 for infinite particle densities to the single-particle case, $w_x^{(\min)} = -\eta v_K$ for $\tau_s = 1.0$ and $w_x^{(\min)} \simeq -0.2\eta v_K$ for $\tau_s = 0.1$. The actual velocity range extends beyond these limits in the turbulent state.

First consider the marginally coupled runs (left column of Fig. 16). The velocity distribution is non-Gaussian with a clear negative skewness (velocities drop sharply at the right side of the Gaussian, with a more gradual decline toward negative velocities). The gray lines show the expected trend of slower inward drift for higher ambient densities. For particles moving radially outward with $v_x > 0$, the average particle density drops with increasing speed. This is reasonable behavior since low density particle clumps can more readily be fed angular momentum

and pushed outward by gas fluctuations.¹¹ The extended tails of fast-drifting material at low densities are responsible for the modest (or non-existent for BC) reduction of drift velocities, despite the slowing, or even reversal, of motion in overdense regions.

Now consider the tightly coupled runs in the right column of Fig. 16. The velocity distributions are nearly Gaussian and extend well beyond the range of laminar drift velocities, indicating that turbulent fluctuations dominate. The peaks are shifted leftward, which produces the higher turbulent drift speeds of Table 2. The gray curves plot the astounding fact that overdense regions drift in faster, a reversal of the laminar trend. This is seen in the movie of AB where dense clumps snake their way inwards while underdense diffuse material races out (the snake patterns are visible in Fig. 5 as well).

5.1.1. Effective Drag on Clumps

The tendency for faster migration of dense clumps for $\tau_s = 0.1$ can be understood as a consequence of an effective, macroscopic drag force acting on the clumps. The gas inside the clump is tied to the clump, but exterior gas passes freely around the surface, exerting an effective drag. If the effective friction time of the clump is closer to unity than the original τ_s , then the dense clump will behave more like a marginally coupled solid and drift inward faster. This collective drag effect is similar to the plate drag model of Ekman layers on the surface of particle subdisks (Goldreich & Ward 1973; Goodman & Pindor 2000).

We estimate the friction time $\tau_f^{(\text{eff})}$ of a clump of radius R_{clump} as the time required to encounter its own mass, M_{clump} , in gas.¹² That gives for 3-D clumps (2-D clumps give the same final scaling)

$$\tau_f^{(\text{eff})} \sim \frac{M_{\text{clump}}}{\rho_g R_{\text{clump}}^2 \Delta v} \sim \frac{\rho_p R_{\text{clump}}}{\rho_g \Delta v}, \quad (7)$$

where ρ_p is the bulk particle density inside the clump and Δv is the speed of the clump relative to the gas. Multiplying each side by Ω yields

$$\Omega \tau_f^{(\text{eff})} \sim \frac{\rho_p R_{\text{clump}}}{\rho_g \eta r} \frac{\eta v_K}{\Delta v}. \quad (8)$$

If we dare test this heuristic hypothesis, reading the size of the clumpy plateaus from Figs. 5 and 7 and the bulk density and speed of the dense clumps relative to the gas from Fig. 16, we find for run AB the values $\rho_p / \langle \rho_g \rangle \approx 2.5$, $R_{\text{clump}} / (\eta r) \approx 0.1$, $\Delta v \approx \eta v_K$ (the velocity difference between high density material and low density material in Fig. 16), corresponding to an effective friction time of $\Omega \tau_f^{(\text{eff})} \approx 0.25$. Run AC has $\rho_p / \langle \rho_g \rangle \approx 6$, $R_{\text{clump}} / (\eta r) \approx 0.05$, $\Delta v \approx \eta v_K$, yielding a very similar value of $\tau_f^{(\text{eff})} \approx 0.3$. Thus our crude estimates show that the clumps couple aerodynamically to the gas more loosely than the individual particles do, explaining at least qualitatively the faster drift of dense clumps and the increase in drag dissipation, two surprising features of the $\tau_s = 0.1$ runs.

¹¹ In the absence of fluctuations and with an outwardly decreasing pressure, particles only drift inwards.

¹² This is the valid criterion for high Reynolds number, turbulent drag.

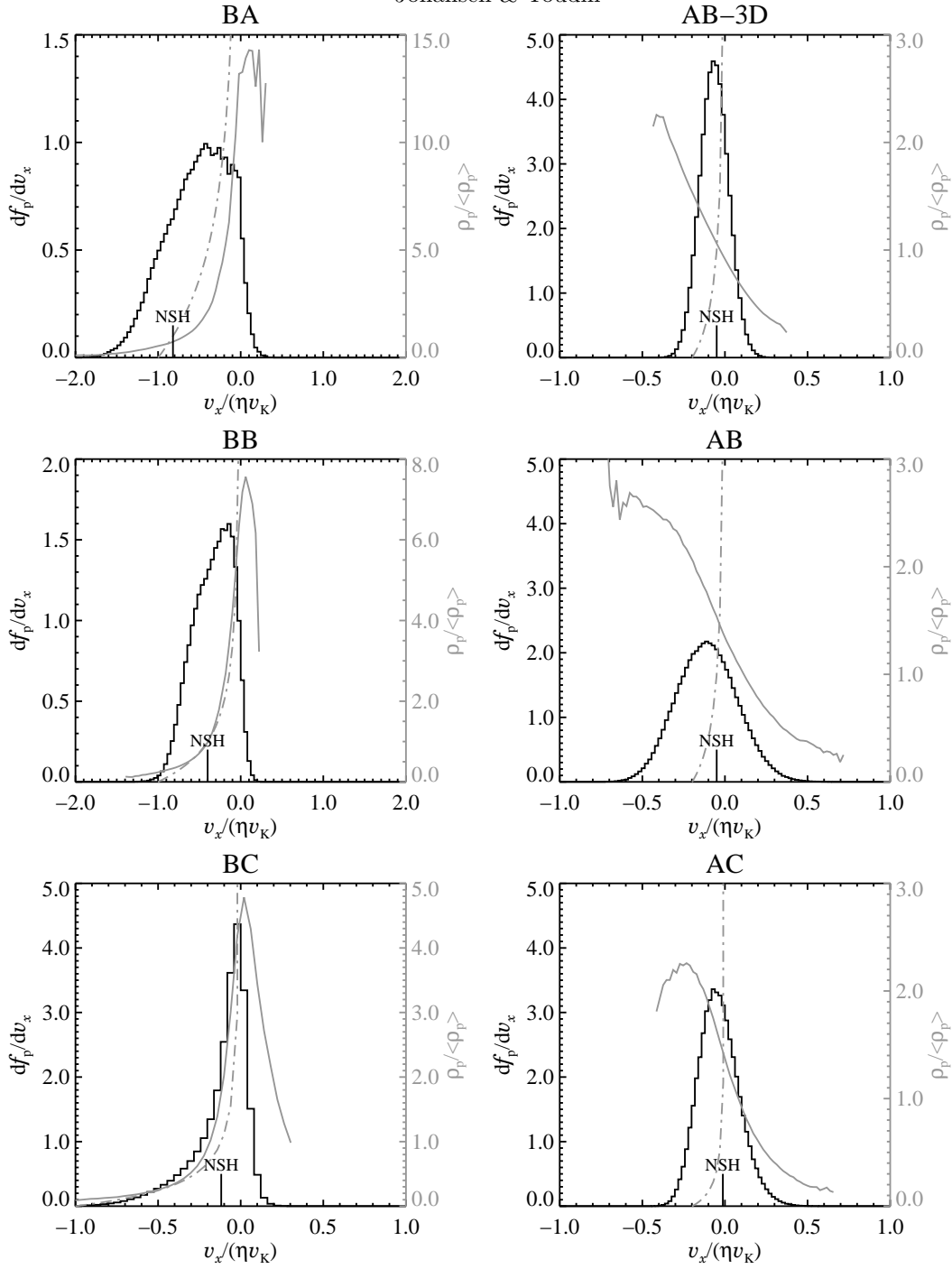


FIG. 16.— Histograms of the fraction of particles with a given radial drift velocity v_x in the turbulent state (black curves). The short vertical lines (labeled NSH) indicate analytical drift velocities in the initial state with no turbulence or clumping. Marginally coupled (B*) runs show a slowing of the net drift speed, whereas tightly coupled runs (A*) produce faster infall. The gray lines (following the right y-axes) show the average particle density in each velocity bin. For reference the gray dash-dotted lines plot the laminar particle density vs. drift velocity relation. The B* runs display the expected decrease in drift speeds with increasing density, whereas the A* runs (surprisingly) follow the opposite trend.

5.2. Momentum Flux

The radial flux of orbital momentum, $\mathcal{F}_{\mathcal{L},x} = \rho_g u_x u_y + \rho_p w_x w_y$, and its contribution to disk heating are discussed in YJ §5. For laminar flow the drag equilibrium between solids and gas gives (equation 18b of YJ)

$$\mathcal{F}_{\mathcal{L},x}^{(\text{NSH})} = -2\tau_s^3 \rho_p \left[\frac{\eta v_K}{(1 + \epsilon)^2 + \tau_s^2} \right]^2. \quad (9)$$

The *inward* transport of angular momentum follows from the the slower rotation of the outgoing gas and the faster rotation of the incoming particles. The values for $\mathcal{F}_{\mathcal{L},x}$ in the saturated turbulent flow are given in Table 3 and are decomposed as $\mathcal{F}_{\mathcal{L},x} = \mathcal{F}_{\mathcal{L},x}^{(\text{NSH})} + \mathcal{F}_{\mathcal{L},x}^{(\text{turb})}$, i.e. the laminar value and changes caused by turbulence. If the turbulence were driven by orbital shear, which releases free energy via outward angular momentum trans-

port, $\mathcal{F}_{\mathcal{L},x}^{(\text{turb})}$ would be positive. Instead, most runs have $\mathcal{F}_{\mathcal{L},x}^{(\text{turb})} < 0$, which is physically allowed since work done by the global pressure gradient powers streaming turbulence. Only run BA (and BA-3D) has $\mathcal{F}_{\mathcal{L},x}^{(\text{turb})} > 0$, but the net angular momentum flux is still inward. Thus in all our simulations, angular momentum transport acts to take kinetic energy out of the motion, at the rate $\dot{\mathcal{E}}_{\mathcal{L}} = (3/2)\Omega\mathcal{F}_{\mathcal{L},x} < 0$ (see YJ §5). As in any shearing box simulation with (shear) periodic boundary conditions, momentum fluxes are divergence-free constants, which prohibits secular evolution. Global simulations are needed to fully investigate the role of “backwards” angular momentum transport from streaming turbulence on disk evolution.

5.3. Turbulent Diffusion

The turbulent mixing of particles is usually modeled as a diffusive process in which particle motions are described by a random walk for large length-scales and over long time-scales. We provide here best fits to the diffusion coefficients in the radial and vertical directions. Since the motion of particles is very complex, and furthermore the particles are not passive contaminants but the cause of turbulence, we also test the validity of the diffusion approximation.

We track the deviation of particle positions, $x_i(t)$ and $z_i(t)$, from their positions at an initial time t_0 when turbulence has already developed. Here we are not concerned with the net radial drift of particles, but the spreading of the distribution $x_i(t) - x_i(t_0)$ (and similarly for vertical motions, although no systematic motion over long time-scales is expected in this direction). Particles are allowed to move greater distances than the box size by deconvoluting any particles that were transferred over the periodic boundaries by the code. For pure diffusion, the distribution tends to a Gaussian with a variance, σ^2 , that grows linearly with time.¹³ An example of how the particles spread out with time is shown in Fig. 17 for radial mixing in the BA simulation. The diffusion coefficients, D_x and D_z , are extracted as

$$D_{x,z} \equiv \frac{1}{2} \frac{\partial \sigma_{x,z}^2}{\partial t}. \quad (10)$$

The best fit diffusion coefficients are listed in Table 3, using the standard normalization by $c_s^2\Omega^{-1}$. The dimensionless diffusion coefficients lie in the interval $10^{-7} \dots 10^{-2}$, ranging from extremely small up to values that are comparable to the diffusion caused by magnetorotational turbulence (Carballido et al. 2005; Johansen & Klahr 2005). For the smaller $\tau_s = 0.1$ particles the diffusion is quite weak, $< 5 \times 10^{-5}$. This is because more tightly coupled particles trigger weaker turbulence with smaller length scales, a result consistent with smaller linear growth rates and wavelengths for lower τ_s (see YG). Run BA ($\tau_s = 1.0, \epsilon = 0.2$) exhibits anomalously large diffusion, especially in the vertical direction, $D_z \approx 0.01$. This is due to the significant bulk motion of elongated clumps (discussed in §3.2).

¹³ Since particles are allowed to cross the periodic boundaries, at late times different portions of the distribution will overlap. This just means that only turbulent scales up to a certain length scale are considered, something that should not significantly affect the integrity of the measurements.

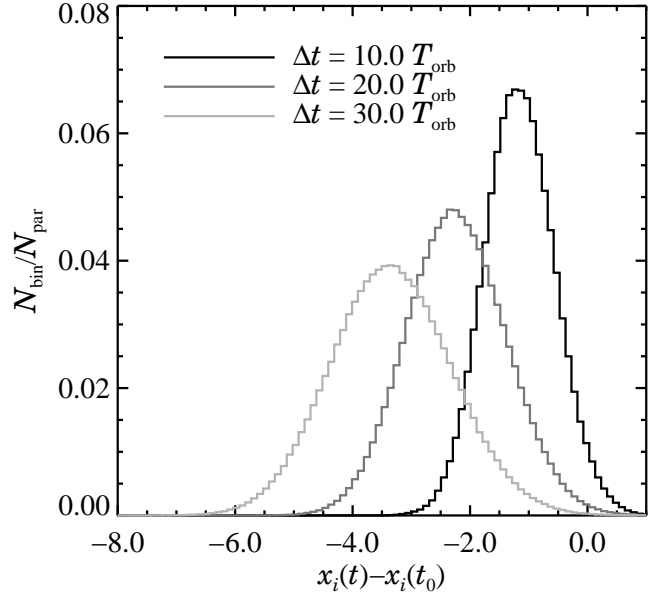


FIG. 17.— Spot the platypus. The histograms plot the radial distance that particles in run BA have traveled since the reference time of $t_0 = 20T_{\text{orb}}$. The curve moves inward due to the radial drift, while spreading as a random walk with a Gaussian width σ that increases as the square root of time. The Gaussians are slightly platykurtic, or flat-tailed, due to a population of solid particles that experience decreased diffusion in the massive particle clumps seen in Fig. 2.

The upper limit for the diffusion appears to be set by the characteristic length and velocity scales, ηr and ηv_K , to be $D \lesssim \eta^2 v_K r \approx \eta c_s^2 / \Omega$, i.e. $D \lesssim \eta = 5 \times 10^{-3}$ when non-dimensionalized. Indeed even the extreme D_z in run BA only violates this order of magnitude criterion by a factor of three. As a consistency check on the diffusion coefficients, $D_{x,z} \approx \delta w_{x,z}^2 t_{\text{corr}}$ is obeyed within a factor of a few, for random velocities, $\delta \mathbf{w}$, from Table 2 (for the gas, but particle values are not more than $\sim 10\%$ different) and the correlation times, t_{corr} , from Fig. 13.

It will be interesting to compare these results to stratified disk models with self-consistent vertical settling, where the relevant parameters are τ_s and the solids-to-gas *surface density ratio* (instead of ϵ).

5.3.1. Validity of the Diffusion Approximation

We performed several tests of the diffusion approximation. The time variation of the diffusion coefficients should be small, and especially should lack an overall deviation from $\partial \sigma^2 / \partial t \propto \text{constant}$. This was true for most runs, as indicated by the error bars on the diffusion coefficients in Table 3. The two exceptions were again run BA, which exhibited large fluctuations due to the interactions between a few large particle clumps, and the two-fluid run AA. This run was seeded with tracer particles, following the velocity field of the solid fluid, in order to be able to use the random walk approach to measure diffusion. The tracer particles exhibited extremely small diffusion with a huge fluctuation interval, an effect of the weak non-linear state of run AA where periodic bulk motion of a few clumps dominates over random motion (see Fig. 7). Particles spread out and gather again in a way that is distinctly not a random walk, but over longer time-scales the particle distribution still spread

out as a Gaussian. The enormous error interval indicates that the turbulent transport is not like diffusion on short time-scales.

We also tested Gaussianity by measuring the skewness and kurtosis of the particle displacement distributions. Most runs were fairly Gaussian, except for a modest skewness, $\sim 10\%$, in the radial (and not vertical) distributions, which is readily explained by the interaction of the radial drift flow with clumps. The BA run exhibited a kurtosis of -0.5 , i.e. slightly platykurtic or small-tailed (see Fig. 17), consistent with transport influenced by bulk motions, and not just a random walk. Modeling turbulent transport as diffusion is under all circumstances only an approximation. Still, the turbulent diffusion coefficient is a good measure of the time-scale on which solid particles are mixed by the turbulent motion.

6. SUMMARY

In this paper we have shown that solid particles can trigger turbulence in gaseous protoplanetary disks via the streaming instability and thereby cause their own clumping. We have ignored a number of complicating effects. Most critical is perhaps the lack of vertical gravity, but we believe it was instructive to see how the streaming instability evolves in a pure model that has exact linear solutions first. We plan to include both vertical gravity and the self-gravity of the solids in a future research project. A distribution of particle sizes and physical collisions between particles have also been ignored, even though coagulation, fragmentation, and collisional cooling are likely relevant in dense particle clumps. As the complex behavior of our simple model system shows, significant progress on basic physical processes can be made before the “kitchen sink” approach is required.

The most striking consequence of streaming turbulence is the growth of overdense particle clumps without self-gravity. This effect was previously seen in the non-linear simulations of particle settling and Kelvin-Helmholtz turbulence by Johansen et al. (2006a). In both that work and this one, clumping can be a self-propagating phenomenon. The increased inertia in dense clumps decreases their drift speeds, creating local “traffic jams.” We saw this behavior for marginally coupled solids, which developed the largest relative overdensities, above 100, with an upward cascade to long-lived, vertically elongated filaments. Marginally coupled solids have the highest radial drift speed and are known to exhibit the most pronounced drag-related phenomena, so it is not surprising that marginal coupling also gives rise to the most dramatic streaming turbulence. While clumping may not in itself explain how to keep large amounts of marginally coupled particles at large orbital distances (Wilner et al. 2000), it does provide a rigorous prediction that the spatial distribution of such solids will not be smooth, but will vary on scales of around one gas scale-height.

A qualitatively different clumping behavior was seen for smaller, more tightly coupled solids. Overdensities

were lower, in the tens, and clumps were smaller scale and short-lived. To extend the analogy, these runs appeared more like a game of bumper cars than a full-scale traffic jam. The biggest surprise was the complete reversal of the laminar relation between drift speed and particle density. Dense clumps actually fell in faster than particles in voids for the tightly coupled solids. Our heuristic explanation is that robust clumps can withstand turbulent boundary layer flows that sap their angular momentum, as in an Ekman layer flow. A similar explanation has been applied to the surfaces of particle sub-disks as the plate drag *ansatz* (Goldreich & Ward 1973; Goodman & Pindor 2000; Weidenschilling 2003). The run with the tightest coupling and lowest initial solids-to-gas density ratio, and consequently the lowest linear growth rate, developed very meek non-linear density fluctuations. Thus non-linear clumping appears to require either marginal coupling or a moderately large background solids-to-gas ratio of around unity or higher. Further studies of the streaming instability for smaller particles, such as chondrules, would be interesting, but are computationally costly (see §3.3).

It is hardly surprising that the solids-to-gas density ratio strongly affects the non-linear state since the streaming instability relies on particle feedback to influence gas dynamics. However, the sharp transition across particle-gas equality is remarkable, especially for tight coupling – the weak streaming instabilities in the gas-dominated regime become explosive once the solids-to-gas ratio reaches unity. Youdin & Shu (2002) argued that this threshold also sets a limit to the quantity of solids that can be stirred by the Kelvin-Helmholtz instability. Vigorous turbulence (if stronger than particles themselves can stir) could prevent the accumulations of such high midplane particle densities. There is little doubt, however, that dramatic events occur whenever particle densities reach that of the gas.

Planetesimal formation models generally involve either high particle densities, in a gravitational collapse scenario, or efficient coagulation to particle sizes for which radial drift is no longer a problem. Both scenarios involve conditions – high particle densities and/or marginal drag force coupling – where streaming instabilities can abet further growth towards planetesimals by generating overdense clumps in the particle component.

The authors would like to thank Jim Stone, Jeremy Goodman, Hubert Klahr and Patrick Glaschke for inspiring discussions and an anonymous referee for comments and suggestions that helped improve the original manuscript. A.J. is grateful to the Annette Kade Graduate Student Fellowship Program at the American Museum of Natural History. A.Y. acknowledges support NASA grant NAG5-11664 issued through the Office of Space Science.

Facilities: RZG (PIA)

REFERENCES

- Barge, P., & Sommeria, J. 1995, *A&A*, 295, L1
 Barranco, J. A., & Marcus, P. S. 2005, *ApJ*, 623, 1157
 Brandenburg, A. 2003, *Computational aspects of astrophysical MHD and turbulence (Advances in Nonlinear Dynamics)*, 269–+
 Brauer, F., Dullemond, C., Johansen, A., Henning, Th., Klahr, H., & Natta, A., submitted to *A&A*
 Carballido, A., Stone, J. M., & Pringle, J. E. 2005, *MNRAS*, 358, 1055

- Carballido, A., Fromang, S., & Papaloizou, J. 2006, *MNRAS*, 373, 1633
- Cuzzi, J. N., Hogan, R. C., Paque, J. M., & Dobrovolskis, A. R. 2001, *ApJ*, 546, 496
- Draine, B. T. 2006, *ApJ*, 636, 1114
- Dubrulle, B., Morfill, G., & Sterzik, M. 1995, *Icarus*, 114, 237
- Dullemond, C. P., & Dominik, C. 2005, *A&A*, 434, 971
- Fessler, J. R., Kulick, J. D., & Eaton, J. K. 1994, *Physics of Fluids*, 6, 3742
- Fromang, S., & Nelson, R. P. 2005, *MNRAS*, 364, L81
- Fromang, S., & Papaloizou, J. 2006, *A&A*, 452, 751
- de la Fuente Marcos, C., & Barge, P. 2001, *MNRAS*, 323, 601
- Goldreich, P., & Ward, W. R. 1973, *ApJ*, 183, 1051
- Goldreich, P. & Tremaine, S. 1978, *ApJ*, 222, 850
- Goodman, J., Narayan, R., & Goldreich, P. 1987, *MNRAS*, 225, 695
- Goodman, J., & Pindor, B. 2000, *Icarus*, 148, 537
- Goodman, J., & Xu, G. 1994, *ApJ*, 432, 213
- Haghighipour, N., & Boss, A. P. 2003, *ApJ*, 598, 1301
- Hayashi, C. 1981, *Prog. Theor. Phys.*, 70, 35
- Hockney, R. W., & Eastwood, J. W. 1981, *Computer Simulation Using Particles* (Computer Simulation Using Particles, New York: McGraw-Hill, 1981)
- Johansen, A., Andersen, A. C., & Brandenburg, A. 2004, *A&A*, 417, 361
- Johansen, A., & Klahr, H. 2005, *ApJ*, 634, 1353
- Johansen, A., Henning, T., & Klahr, H. 2006a, *ApJ*, 643, 1219
- Johansen, A., Klahr, H., & Henning, T. 2006b, *ApJ*, 636, 1121
- Johansen, A., Klahr, H., & Mee, A. J. 2006c, *MNRAS*, 370, L71
- Klahr, H. H., & Bodenheimer, P. 2003, *ApJ*, 582, 869
- Klahr, H. H., & Lin, D. N. C. 2001, *ApJ*, 554, 1095
- Nakagawa, Y., Sekiya, M., & Hayashi, C. 1986, *Icarus*, 67, 375
- Padoan, P., Cambr esy, L., Juvela, M., Kritsuk, A., Langer, W. D., & Norman, M. L. 2006, *ApJ*, 649, 807
- Rice, W. K. M., Lodato, G., Pringle, J. E., Armitage, P. J., & Bonnell, I. A. 2004, *MNRAS*, 355, 543
- Rodmann, J., Henning, T., Chandler, C. J., Mundy, L. G., & Wilner, D. J. 2006, *A&A*, 446, 211
- Safronov, V. S. 1969, *Evolutsiia doplanetnogo oblaka*. (Moscow: Nauka)
- Stepinski, T. F., & Valageas, P. 1996, *A&A*, 309, 301
- Takeuchi, T., & Lin, D. N. C. 2002, *ApJ*, 581, 1344
- Turner, N. J., Willacy, K., Bryden, G., & Yorke, H. W. 2006, *ApJ*, 639, 1218
- Ward, W. R. 1976, in *Frontiers of Astrophysics*, ed. E.H. Avrett, 1–40
- Ward, W. R. 2000, in *Origin of the Earth and Moon*, 75–84
- Weidenschilling, S. J. 1977a, *MNRAS*, 180, 57
- . 1977b, *Ap&SS*, 51, 153
- . 2003, *Icarus*, 165, 438
- Wilner, D. J., Ho, P. T. P., Kastner, J. H., & Rodr iguez, L. F. 2000, *ApJ*, 534, L101
- Youdin, A. N. 2005a, *astro-ph/0508659*
- . 2005b, *astro-ph/0508662*
- Youdin, A. N., & Chiang, E. I. 2004, *ApJ*, 601, 1109
- Youdin, A. N., & Goodman, J. 2005, *ApJ*, 620, 459
- Youdin, A. N., & Johansen, A. 2007, *ApJ*
- Youdin, A. N., & Shu, F. H. 2002, *ApJ*, 580, 494